

Supplementary Material for
“A Mechanistic Model of Annual Sulfate Concentrations in the U.S.”

Nathan B. Wikle¹, Ephraim M. Hanks², Lucas R.F. Henneman³, and Corwin M. Zigler¹

¹Department of Statistics and Data Sciences, University of Texas at Austin

²Department of Statistics, Pennsylvania State University

³Department of Civil, Environmental, and Infrastructure Engineering, George Mason
University

December 1, 2021

Contents

1	Numerical Methods for Approximating Continuous Processes in Discrete Space	2
1.1	Step One: Discretization	2
1.2	Step Two: Numerical Approximation of \mathcal{A}	3
1.3	Atmospheric Sulfate Process	5
2	A Sensitivity Analysis of the FVM Grid Size	6
2.1	The Initial Grid Choice	6
2.2	Results	6
3	Wind Velocity	10
4	A Phenomenological Spatial Model of Annual Sulfate Concentrations	11

1 Numerical Methods for Approximating Continuous Processes in Discrete Space

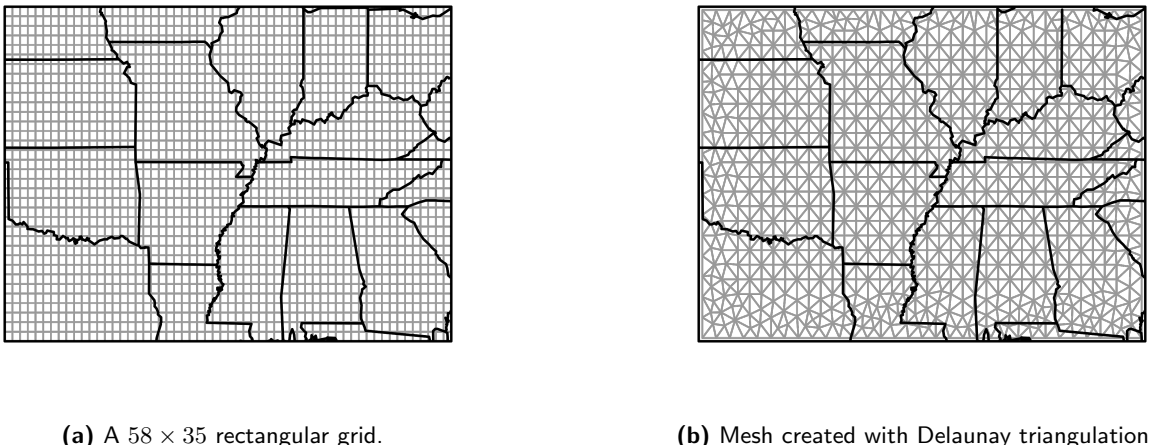
Consider the continuous space-time stochastic process introduced in Section 3.1,

$$dy_s(t) = \left(-\mathcal{A}_s(\theta)y_s(t) + m_s(\theta) \right) dt + \mathcal{B}_s(\theta) \xi(s, t), \quad (\text{SM.1})$$

where $y_s(t)$ ($s \in \mathcal{D} \subset \mathbb{R}^2$, $t \geq 0$) is the quantity of interest, \mathcal{A}_s is a linear operator, m_s denotes a source/sink at location s , and $\mathcal{B}_s \xi(s, t)$ is a space-time white noise process, with process variance defined by real-valued function \mathcal{B}_s . For convenience, we will assume that this process has constant variance, i.e., $\mathcal{B}_s \equiv \sigma$ for all s . As discussed in our manuscript, it is often useful to define a dynamic process as an SPDE in continuous space. However, the theoretical and computational limitations associated with working in continuous space-time necessitates an approximation of (SM.1) in discrete space. This supplementary document provides a brief overview of how we implement such an approximation. Particular attention is focused on the sulfate model presented in the manuscript (see Sections 2 and 4 of the manuscript for details).

1.1 Step One: Discretization

The numerical representation of (SM.1) in discrete space occurs in two steps. First, the continuous surface $\mathcal{D} \subset \mathbb{R}^2$ must be appropriately *discretized* to some finite collection of points, $\mathcal{S} = \{s_1, \dots, s_k\}$. Second, the mathematical operator \mathcal{A} is *approximated with a matrix operator*, \mathbf{A} , on the set of discretized points, \mathcal{S} . The resulting stochastic process, defined on discrete space \mathcal{S} , is a computationally convenient representation of the original dynamic process defined in continuous space.



(a) A 58×35 rectangular grid.

(b) Mesh created with Delaunay triangulation.

Figure 1: Example discretizations of the surface, \mathcal{D} , considered in the sulfate analysis, including (a) a simple rectangular grid, and (b) a more complex Delaunay triangulation (created with the R-INLA package [4]).

The discretization step is conceptually simple. A grid or polygonal *mesh* is overlaid on top of the continuous surface, \mathcal{D} , and the process dynamics are defined with respect to the discrete set of mesh cells. The structure of the mesh may vary, from a simple rectangular grid (Figure 1a) to more complex structures, such as those generated via Delaunay triangulation (Figure 1b). The choice of mesh structure is often dictated by the complexity of the process dynamics, the boundary

of the surface \mathcal{D} , and the chosen numerical approximation scheme (for example, finite element method implementations often use a triangulation method). Because of the variety of discretization schemes, and the large body of literature discussing their relative merits [3, 8, 1], we encourage the interested reader to explore implementation details tailored to their problem of interest. For now, we emphasize that the discretization step restricts the process of interest to some discrete set of points, $\mathcal{S} = \{\mathbf{s}_1, \dots, \mathbf{s}_n\}$, corresponding to mesh vertices and/or centroids.

1.2 Step Two: Numerical Approximation of \mathcal{A}

After a suitable mesh has been chosen, process dynamics are approximated on the discretized space, \mathcal{S} . A variety of numerical schemes have been developed to facilitate this approximation, including the finite difference method (FDM), finite volume method (FVM), and finite element method (FEM). Again, the literature and implementation for each of these methods are too extensive and problem-specific to permit a comprehensive introduction to these methods, and we encourage the interested reader to consult one of the following references for implementation details [3, 8, 1]. We instead emphasize that each method attempts to approximate a continuous mathematical operator, \mathcal{A} , with a discrete operator, \mathbf{A} , defined on the discretized space, \mathcal{S} . These approximations may occur via simple comparisons of neighboring values (such as first and second differences), or via the construction of appropriate basis functions; the implementation is dependent on the problem of interest and choice of numerical method.

As an example, consider the operator,

$$\mathcal{A} = \gamma\Delta + \alpha \mathbf{v}_i(t) \cdot \nabla - \delta, \quad (\text{SM.2})$$

corresponding to the advection-diffusion process used to model sulfate concentration in Section 2.1 (Equation (1) of the manuscript). Here, $\gamma\Delta$ denotes homogeneous spatial diffusion with rate γ (note, $\Delta \equiv \frac{\partial^2}{\partial x_1^2} + \frac{\partial^2}{\partial x_2^2}$); advection due to wind is defined by the advective derivative $\mathbf{v}_i(t) \cdot \nabla \equiv v_{x_1} \frac{\partial}{\partial x_1} + v_{x_2} \frac{\partial}{\partial x_2}$, where $\mathbf{v}_i(t) = (v_{x_1}, v_{x_2})'$ is the velocity vector at time t ; and atmospheric deposition occurs at rate δ . A simple numerical approximation of this operator might be constructed in the following way.

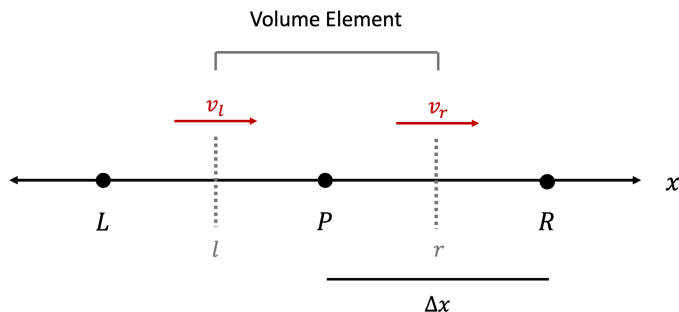


Figure 2: Example discretization (regular grid, one dimension) at three points: L , P , and R . The process $Y(x, t)$ evaluated at these points is used for the second-order central difference approximation to diffusion and the FVM upwind scheme for advection-diffusion.

Let $\mathcal{A}_1 \equiv \gamma\Delta$ denote homogeneous diffusion with rate γ , which for a process $Y(x, t)$ defined in

one-dimensional space x can be equivalently written as,

$$\mathcal{A}_1 Y = \frac{\partial}{\partial x} \left(\gamma \frac{\partial Y}{\partial x} \right). \quad (\text{SM.3})$$

How might we approximate this operator on some set of regular discrete points, \mathcal{S} ? Consider three points, P , $R = P + \Delta x$, and $L = P - \Delta x$, and assume the process Y can be evaluated at each point at time t : i.e., $Y(P, t)$, $Y(R, t)$, and $Y(L, t)$. These correspond to three discrete points in our discretization, \mathcal{S} (Figure 2). A second-order difference approximation of \mathcal{A}_1 can be constructed by first recognizing that the first derivative, $\frac{\partial Y(P,t)}{\partial x}$, can be approximated with simple linear differences,

$$\left[\frac{\partial Y(P, t)}{\partial x} \right]_R \approx \frac{Y(P + \Delta x, t) - Y(P, t)}{\Delta x} = \frac{Y(R, t) - Y(P, t)}{\Delta x} \quad (\text{SM.4})$$

and

$$\left[\frac{\partial Y(P, t)}{\partial x} \right]_L \approx \frac{Y(P, t) - Y(P - \Delta x, t)}{\Delta x} = \frac{Y(P, t) - Y(L, t)}{\Delta x}. \quad (\text{SM.5})$$

Then, using (SM.4) and (SM.5), we have

$$\mathcal{A}_1 Y(P, t) \equiv \frac{\partial}{\partial x} \left(\gamma \frac{\partial Y(P, t)}{\partial x} \right) \quad (\text{SM.6})$$

$$\approx \left(\gamma \left[\frac{\partial Y(P, t)}{\partial x} \right]_R - \gamma \left[\frac{\partial Y(P, t)}{\partial x} \right]_L \right) / \Delta x \quad (\text{SM.7})$$

$$= \gamma \frac{Y(R, t) - 2Y(P, t) + Y(L, t)}{(\Delta x)^2}. \quad (\text{SM.8})$$

Repeating this process for all points in \mathcal{S} , we can now approximate the operator $\mathcal{A}_1 Y$ in discrete space as,

$$\mathcal{A}_1 \mathbf{Y}_t = \gamma \begin{pmatrix} \ddots & \ddots & \ddots & & \\ & 1 & -2 & 1 & \\ & \ddots & \ddots & \ddots & \end{pmatrix} \begin{pmatrix} \vdots \\ Y(L, t) \\ Y(P, t) \\ Y(R, t) \\ \vdots \end{pmatrix}. \quad (\text{SM.9})$$

Note that \mathcal{A}_1 is a sparse, banded matrix, which permits computationally efficient matrix operations [5] when working with the discrete space model.

The above discretization of a diffusion operator can be derived using either the finite difference method or the finite volume method [8]. However, the addition of advection due to wind necessitates a slightly more complex discretization scheme, as centered difference approximations become increasingly biased towards upstream process values as advective forces grow large [8]. Instead, we use an upwind differencing scheme to approximate advection-diffusion with the FVM. In short, for our three points, P , $R = P + \Delta x$, and $L = P - \Delta x$, we evaluate (or estimate) the wind velocity $v(x, t)$ along volume element faces l and r (i.e., $v_l \equiv v(l, t)$ and $v_r \equiv v(r, t)$; see Figure 2). Then, the operator

$$\mathcal{A}_2 Y \equiv \gamma \Delta + \alpha \mathbf{v}_i(t) \cdot \nabla = \frac{\partial}{\partial x} \left(\gamma \frac{\partial Y}{\partial x} \right) + \alpha v(x, t) \frac{\partial Y}{\partial x} \quad (\text{SM.10})$$

can be approximated with

$$\mathbf{A}_2 \mathbf{Y}_t = \gamma \begin{pmatrix} \ddots & \ddots & \ddots & & \\ & a_L & -a_P & a_R & \\ & \ddots & \ddots & \ddots & \end{pmatrix} \begin{pmatrix} \vdots \\ Y(L, t) \\ Y(P, t) \\ Y(R, t) \\ \vdots \end{pmatrix}, \quad (\text{SM.11})$$

where a_L , a_P , and a_R are given in Table 1. Additional details of the FVM upwind differencing scheme can be found in Chapter 5 of Versteeg and Malalasekera [8].

Table 1: Matrix entries for the FVM upwind difference approximation of an advection-diffusion operator.

Edge Velocities	Matrix Entries		
	a_L	a_R	a_P
$v_l > 0, v_r > 0$	$\gamma + \alpha v_l$	γ	$2\gamma + \alpha(v_r - v_l)$
$v_l < 0, v_r < 0$	γ	$\gamma - \alpha v_r$	$2\gamma + \alpha(v_r - v_l)$

Finally, including atmospheric deposition in the process (i.e., $\mathcal{A} = \gamma\Delta + \alpha \mathbf{v}_i(t) \cdot \nabla - \delta$) only requires the subtraction of the deposition rate δ from the matrix diagonal of \mathbf{A}_2 , i.e., $\mathcal{A} \approx \mathbf{A} = \mathbf{A}_2 - \delta\mathbf{I}$. Thus, the advection-diffusion-deposition process found in our manuscript has been approximated in one dimension; the extension of these methods to two dimensions is straightforward [8].

1.3 Atmospheric Sulfate Process

In summary, the approximation of a continuous process in discrete space occurs by first discretizing continuous space \mathcal{D} to discrete space \mathcal{S} , and then approximating the continuous operator \mathcal{A} with its discrete representation, \mathbf{A} , as determined by some numerical scheme such as the FDM, FVM, or FEM. In our manuscript, the continuous process was the region of the continental USA shown in Figure 3. We discretized this space with a 116×70 rectangular grid, represented with black dots in Figure 3. Then, using this discretization, we approximated the advection-diffusion-deposition process, $\mathcal{A} = \gamma\Delta + \alpha \mathbf{v}_i(t) \cdot \nabla - \delta$, with the \mathbb{R}^2 extension of the matrix \mathbf{A} in the previous section. Finally, we let \mathbf{Y}_t denote the vector of sulfate values evaluated at each point in \mathcal{S} (Figure 3), \mathbf{m} a vector of sulfate sources corresponding to each point in \mathcal{S} , and \mathbf{W}_t a vector of independent Brownian motions located at each point in \mathcal{S} . Thus, each continuous element in Equation (SM.1) has a discrete counterpart, and our continuous space-time sulfate process can now be approximated with the multivariate Ornstein-Uhlenbeck (discrete space) process,

$$d\mathbf{Y}_t = (-\mathbf{A}\mathbf{Y}_t + \mathbf{m})dt + \sigma d\mathbf{W}_t. \quad (\text{SM.12})$$

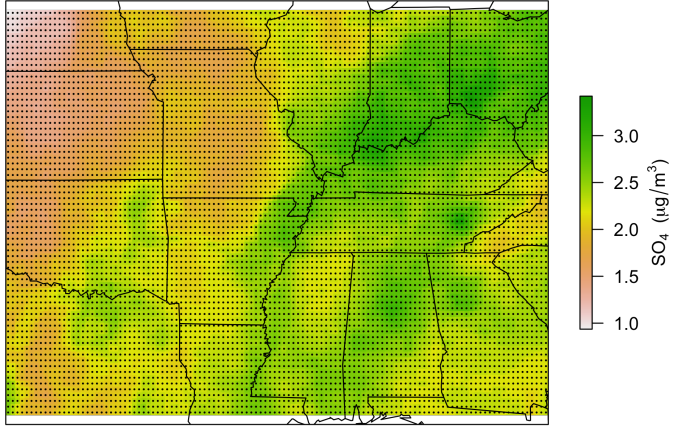


Figure 3: Spatial region \mathcal{D} considered in the sulfate analysis, with the overlaid 70×116 rectangular grid, \mathcal{S} , used in the discrete approximation.

2 A Sensitivity Analysis of the FVM Grid Size

It is important to remember that these numerical methods are *approximations*, and as such, it is reasonable to ask how sensitive the results are to the choice of mesh. We present a short sensitivity analysis of our FVM discretization scheme, focusing on the sensitivity of the inferred mean SO_4 surface and the parameter estimates to the FVM grid size.

2.1 The Initial Grid Choice

As discussed in Section 1.3 (Supp. Material), an FVM approach was used to approximate the system of equations (1–2) describing annual SO_4 concentrations due to SO_2 emissions from power plants. The SO_4 data are state-of-the-art, model-derived surface estimates of annual average sulfate concentrations in the continental United States, available at fine-resolution from the Dalhousie University Atmospheric Composition Analysis Group [6]. When restricted to the geographic region used in our analysis, the full resolution SO_4 surface creates a 1120×1850 rectangular grid ($n = 2,702,000$ cells), with a median cell area of approximately 1 km^2 . With over 2.7 million elements, the full resolution grid is obviously computationally prohibitive — instead, we selected a 70×116 rectangular grid with reduced resolution ($n = 8120$ cells, median cell area $\approx 250 \text{ km}^2$) for our main analysis (Fig 3). The structured rectangular mesh is a direct consequence of the regular locations of the SO_4 data, and the lower-resolution allows for computationally feasible inference.

2.2 Results

The sensitivity of our results to mesh size was compared by repeating the sulfate analysis using twenty different grids, each with a different resolution (Table 2). For each grid, SO_4 data were available at grid nodes (ie, we never had missing data), and SO_2 emissions sources were matched to grid locations. Example grids and corresponding SO_4 surfaces for five example resolutions are shown in the right column of Figure 4.

Table 2: Mesh sizes (and attributes) used in the sensitivity analysis, ordered from coarsest to finest resolution. The mesh used in the original analysis is in bold.

# of cells (n)	width \times length	median cell area (km^2)
522	18 \times 29	4085
589	19 \times 31	3590
680	20 \times 34	3120
792	22 \times 36	2695
936	24 \times 39	2300
1118	26 \times 43	1930
1316	28 \times 47	1590
1664	32 \times 52	1290
2030	35 \times 58	1020
2356	38 \times 62	900
2680	40 \times 67	780
3168	44 \times 72	675
3666	47 \times 78	575
4335	51 \times 85	480
5208	56 \times 93	400
6489	63 \times 103	320
8120	70 \times 116	250
10640	80 \times 133	195
14570	94 \times 155	145
20720	112 \times 185	100

To assess the sensitivity of our results to grid size, we compared the inferred mean SO_4 surface attributed to SO_2 emissions under each grid. Figure 4 shows the inferred mean SO_4 plots, and their corresponding observed 2011 SO_4 surfaces, from the analysis repeated at five different grid resolutions. Despite a dramatic change in grid size (from $n = 522$ to $n = 20,720$), the inferred mean annual SO_4 surfaces are very similar across analyses. In other words, the same underlying process dynamics assumed by our model are consistently estimated across grid size. Thus, we conclude that our results in Section 4, especially those concerning our assessment of human exposure to SO_4 due to individual power plant emissions, are likely invariant to the FVM grid resolution.

Despite the invariance of the inferred mean annual SO_4 concentrations to grid size, the sensitivity of individual parameter estimates to mesh resolution is more pronounced. Figure 5 shows posterior median and 95% credible intervals (CIs) for four parameters from the time-averaged, coupled sulfate model used in our analysis. The inferred parameters are plotted according to the median cell areas of the mesh used in each analysis; they have been rescaled to match the units used in the original analysis. Some of the inferred parameters, such as the rate of SO_2 emissions, β , appear robust to changing grid size (Fig 5a). However, others (such as the standard deviation of the driving noise process, σ) are not constant across grid size, but instead appear to follow a decreasing trajectory as grid resolution increases. Thus, we believe that caution is warranted when interpreting individual parameter values, as the size of the parameter must be interpreted within the context of the grid resolution used in the analysis. Instead, the focus of the analysis should be on the inferred dynamics of the entire process, which we found to be invariant to grid size (Fig 4). The results of our SO_4 analysis discussed in Section 4 of our manuscript largely focus on the (grid-invariant) inferred process dynamics, as we are most interested in the effect of reduced SO_2 emissions on human exposure to SO_4 . Based on this sensitivity analysis, we believe that our choice of grid resolution does not significantly change our results.

Fitted Mean SO₄ Surfaces, Arranged by Grid Size

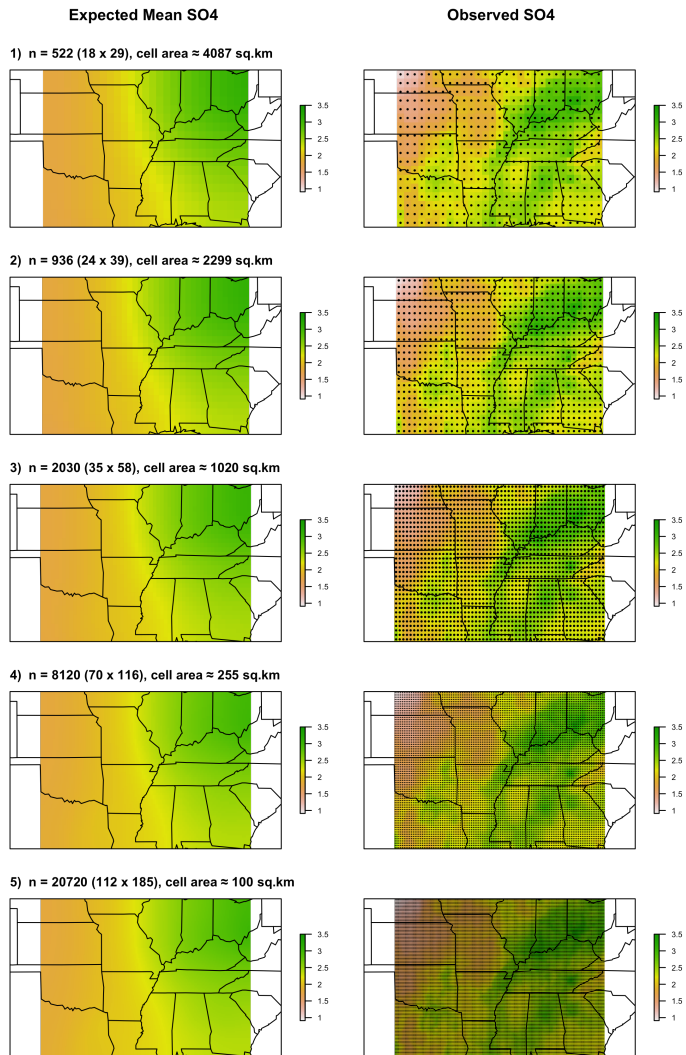


Figure 4: Estimated mean annual SO₄²⁻ from power plant SO₂ emissions, arranged by increasing grid resolution. The inferred mean SO₄ surface is accompanied by a plot of the observed 2011 SO₄ concentrations, with the grid centroids represented as black dots.

Estimated parameter values by grid size (cell area)

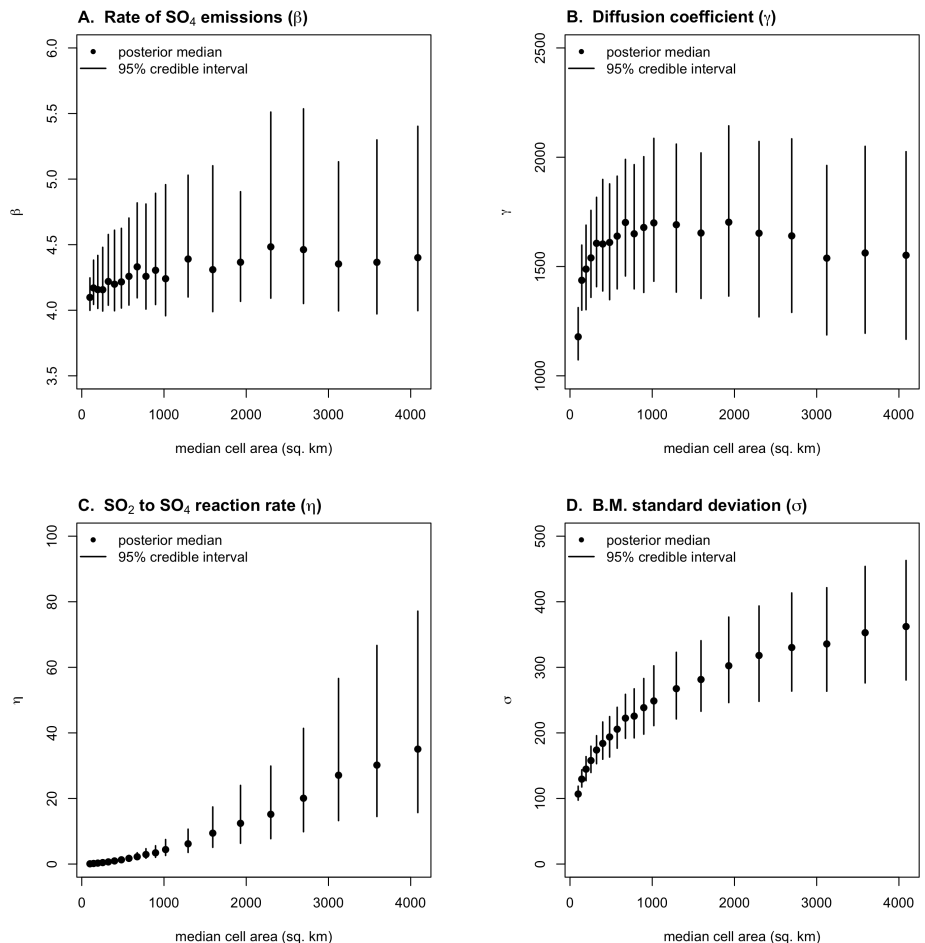


Figure 5: Inferred marginal posterior median and 95% credible intervals for several parameters from the time-averaged, coupled sulfate model used in our analysis. Parameter estimates have been rescaled to match the units used in the original analysis.

3 Wind Velocity

Figure 6 shows the 2011 monthly wind velocity vector fields over the region of the U.S. used in the study. Notice that although some regions exhibit (relatively) constant monthly wind direction (in particular, the top right and bottom left regions), there remains variation in the magnitude of the velocity vectors. Other regions (e.g., the top left and bottom right corners of the map) exhibit more variation in wind direction, and the month of September in particular is an outlier. Possible extensions of our model that would allow for time-varying velocity are discussed in Section 5 of the manuscript.

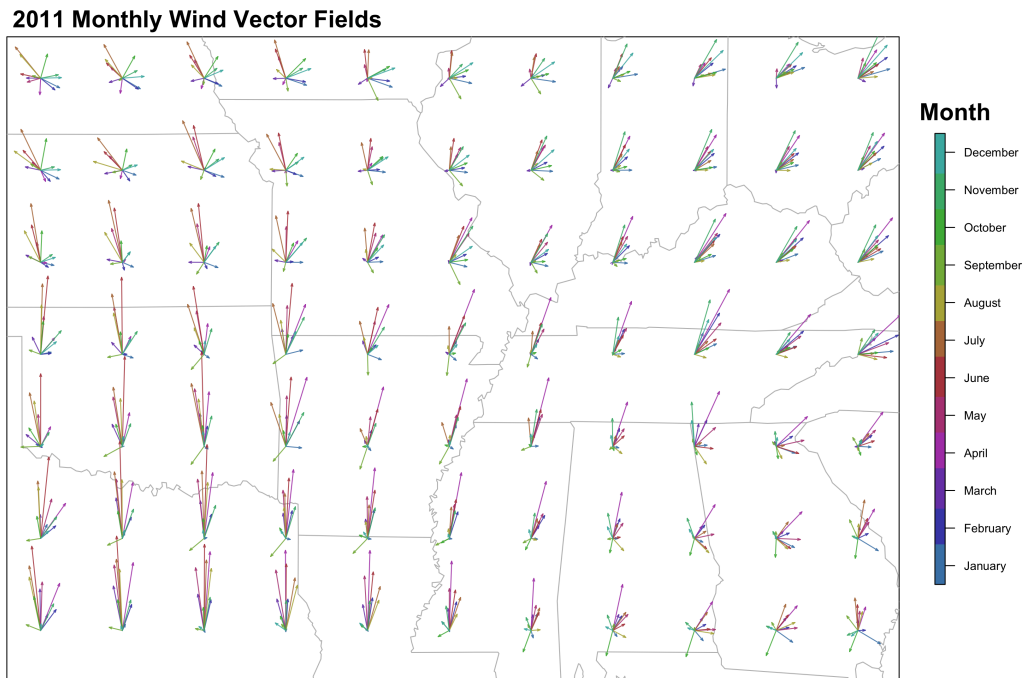


Figure 6: Monthly 2011 wind velocities (height = 10 m), from the NCEP/NCAR reanalysis database [2].

4 A Phenomenological Spatial Model of Annual Sulfate Concentrations

In Section 4.1 of the main text, we compare our best fitting mechanistic model (i.e., the time-averaged, coupled SO₂-SO₄ model) with three alternatives: two other mechanistic models, and a so-called “phenomenological” model. The models are defined as follows:

- **Alternative 1:** a time-averaged spatial model with sulfur dioxide power plant emissions now included as a direct source of SO₄²⁻ (i.e., **no coupling with SO₂**).

Adopting the notation of the main text for $\mathbf{A}_\theta = (\gamma \mathbf{D} + \alpha \mathbf{C} + \delta \mathbf{I})$, θ , and \mathbf{X} , this model is written as

$$\mathbf{y}_1 \sim N(\boldsymbol{\mu}_1(\boldsymbol{\theta}, \mathbf{X}), \boldsymbol{\Sigma}_1), \quad (\text{SM.13})$$

where

$$\boldsymbol{\mu}_1(\boldsymbol{\theta}, \mathbf{X}) = \mathbf{A}_\theta^{-1}(\beta \mathbf{X}) \quad (\text{SM.14})$$

and

$$\boldsymbol{\Sigma}_1 = \frac{\sigma^2}{T} (\mathbf{A}_\theta' \mathbf{A}_\theta)^{-1}. \quad (\text{SM.15})$$

The covariance structure is the same as the best fit model, however the mean is simpler — there is no coupled SO₂-SO₄ system included in this model.

- **Alternative 2:** a stationary ‘snapshot’ model with coupling between SO₄ and SO₂.

This model is similar to the best fit model in its definition of the mean, but with the covariance defined as the solution to the stationary snapshot distribution. Thus, we have

$$\mathbf{y}_2 \sim N(\boldsymbol{\mu}_2(\boldsymbol{\theta}, \mathbf{X}), \boldsymbol{\Sigma}_2), \quad (\text{SM.16})$$

where

$$\boldsymbol{\mu}_2(\boldsymbol{\theta}, \mathbf{X}) = \mathbf{A}_\theta^{-1}(\eta \mathbf{Z}_{\boldsymbol{\theta}, \mathbf{X}}) \quad (\text{SM.17})$$

and

$$\boldsymbol{\Sigma}_2 = \frac{\sigma^2}{2} \mathbf{A}^{-1}. \quad (\text{SM.18})$$

The mean is the deterministic solution to the coupled SO₂-SO₄ system of equations defined by Equations 18 and 19 in the main text, and the covariance has the CAR structure defined by Equation 10.

- **Alternative 3:** a **phenomenological spatial model**, where the mean annual sulfate is modeled as the sum of weighted bivariate Gaussian functions centered at power plant locations, with the weight of each Gaussian function proportional to the facility’s annual emissions total, and the covariance is modeled as a simultaneous autoregressive (SAR) process.

Specifically, this model is our attempt to specify a mean function and a common spatial covariance structure without input from the assumed underlying physical process. The construction of such a model for sulfate concentrations – in particular, of a mean function relating SO₂ emissions to SO₄ – is not immediately obvious. We considered several models, before settling on the following.

Let \mathbf{y}_3 denote the vector of 2011 annual mean sulfate concentrations, observed at points $\mathbf{s}_i \in \mathcal{S}$. Furthermore, $\mathbf{v}_i = (v_{i,x_1}, v_{i,x_2})'$ is the annual mean wind velocity vector at location \mathbf{s}_i , $X(\mathbf{s}_i)$ is the annual SO₂ emissions (in tons) emitted from a power plant located at \mathbf{s}_i ($X(\mathbf{s}_i) = 0$ if no power plant exists at \mathbf{s}_i), and \mathcal{E} denotes the set of spatial locations with coal-fired power plants. Then,

$$\mathbf{y}_3 \sim N(\boldsymbol{\mu}_3, \boldsymbol{\Sigma}_{SAR}), \quad (\text{SM.19})$$

where

$$\mu(\mathbf{s}_i) = \beta_0 + \beta_1 v_{i,x_1} + \beta_2 v_{i,x_2} + f(\mathbf{s}_i|\alpha, \sigma), \quad (\text{SM.20})$$

and

$$f(\mathbf{s}_i|\alpha, \sigma) = \sum_{\mathbf{s}_j \in \mathcal{E}} \alpha \sqrt{\frac{X(\mathbf{s}_j)}{1000}} \exp\left(\frac{-||\mathbf{s}_i - \mathbf{s}_j||}{2\sigma^2 X(\mathbf{s}_j)}\right). \quad (\text{SM.21})$$

Thus, the mean SO₄ concentration at location \mathbf{s}_i is a weighted sum of bivariate Gaussian functions, each centered at power plant locations $\mathbf{s}_j \in \mathcal{E}$, where the mode and width of each function is proportional to the square root of the annual SO₂ total emitted from each power plant, combined with fixed effects ($\beta_0, \beta_1, \beta_2$) corresponding to an intercept and shifts in expected annual sulfate due to the wind velocity at location \mathbf{s}_i . Finally, a simultaneous autoregressive (SAR) covariance structure $\boldsymbol{\Sigma}_{SAR}$ was used to model the second-order structure of the process [7]; no observational error was assumed.

As described in the main text, the phenomenological model has a higher DIC than the best-fitting mechanistic model, and a comparison of the simulated SO₄ surface of the mechanistic model with the phenomenological model (Figure 7) confirms that the mechanistic model best fits the data. In addition, we've included a plot of the model's estimated mean SO₄ due to sulfur dioxide emissions (see Figure 8 below). In summary, modeling the association between mean annual SO₄ concentrations and power plant emissions is challenging without incorporating the underlying dynamics of the system.

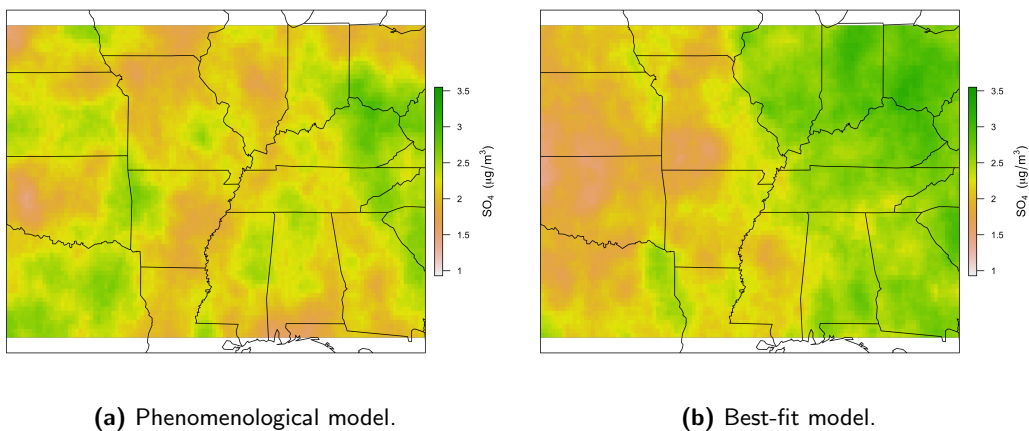


Figure 7: A comparison of simulated annual SO₄ due to sulfur dioxide emissions, from (a) the phenomenological spatial model, and (b) the time-averaged model with coupled SDE (the best-fit model).

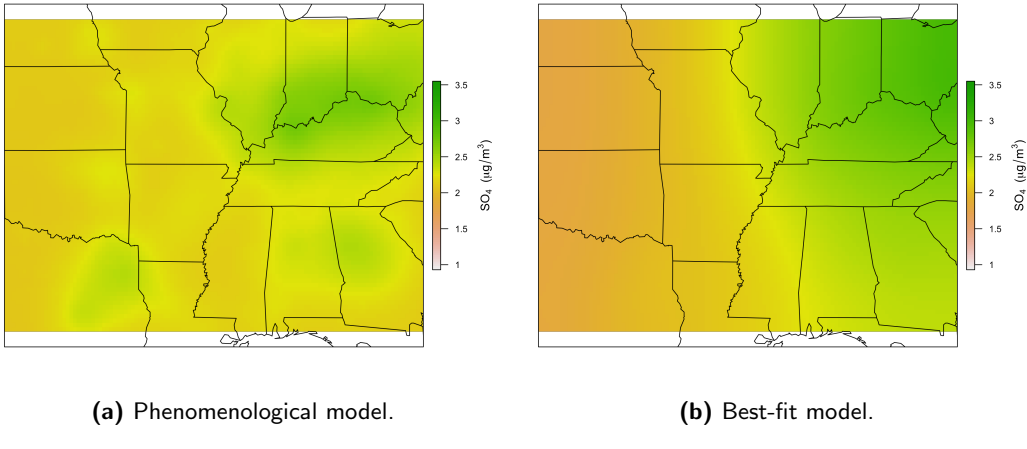


Figure 8: A comparison of the estimated **mean** annual SO_4 due to sulfur dioxide emissions, from (a) the phenomenological spatial model, and (b) the time-averaged model with coupled SDE (the best-fit model).

References

- [1] Claes Johnson. *Numerical solution of partial differential equations by the finite element method*. Dover Publications Inc., New York, 2009.
- [2] E. Kalnay, M. Kanamitsu, R. Kistler, W. Collins, D. Deaven, L. Gandin, M. Iredell, S. Saha, G. White, J. Woollen, Y. Zhu, M. Chelliah, W. Ebisuzaki, W. Higgins, J. Janowiak, K. C. Mo, C. Ropelewski, J. Wang, A. Leetmaa, R. Reynolds, R. Jenne, and D. Joseph. The ncep/near 40-year reanalysis project. *Bull. Amer. Meteor. Soc.*, 77:437 – 470, 1996.
- [3] Hans Petter Langtangen and Svein Linge. *Finite difference computing with PDEs: A modern software approach*. Springer International Publishing, 2017.
- [4] Finn Lindgren and Havard Rue. Bayesian spatial modelling with r-inla. *Journal of Statistical Software, Articles*, 63(19):1–25, 2015.
- [5] Havard Rue and Leonhard Held. *Gaussian Markov random fields: Theory and methods*. Chapman and Hall/CRC, New York, 2005.
- [6] A. van Donkelaar, R. V. Martin, C. Li, and R. T. Burnett. Regional estimates of chemical composition of fine particulate matter using a combined geoscience-statistical method with information from satellites, models, and monitors. *Environmental Science & Technology*, 53(5):2595–2611, 2019.
- [7] J. M. Ver Hoef, E. M. Hanks, and M. B. Hooten. On the relationship between conditional (car) and simultaneous (sar) autoregressive models. *Spatial Statistics*, 25:68 – 85, 2018.
- [8] H. K. Versteeg and W. Malalasekera. *An introduction to computational fluid dynamics: The finite volume method*. Pearson Education Ltd, Harlow, England, 2007.